

22. C. S. Ponce Jr. et al., *J. Am. Chem. Soc.* **136**, 5189–5192 (2014).
 23. See the supplementary materials on Science Online.
 24. C. C. Stoumpos, C. D. Malliakas, M. G. Kanatzidis, *Inorg. Chem.* **52**, 9019–9038 (2013).

ACKNOWLEDGMENTS

The authors acknowledge financial support from the Ministry of Science and Technology of China (863 project, grant no.

SS2013AA50303), the National Natural Science Foundation of China (grant no. 61106056), the Science and Technology Department of Hubei Province (grant no. 2013BAA090), and the Fundamental Research Funds for the Central Universities (grant no. HUSTNY022). We thank the Analytical and Testing Center of Huazhong University of Science and Technology for field emission SEM, TEM, and XRD testing. M.G. thanks the European Research Council for financial support under advanced research grant ARG 247404, "Mesolight."

SUPPLEMENTARY MATERIALS

www.sciencemag.org/content/345/6194/295/suppl/DC1
 Materials and Methods
 Supplementary Text
 Figs. S1 to S9
 References

14 April 2014; accepted 3 June 2014
 10.1126/science.1254763

APPLIED OPTICS

Dielectric gradient metasurface optical elements

Dianmin Lin,^{1*} Pengyu Fan,^{1*} Erez Hasman,² Mark L. Brongersma^{1†}

Gradient metasurfaces are two-dimensional optical elements capable of manipulating light by imparting local, space-variant phase changes on an incident electromagnetic wave. These surfaces have thus far been constructed from nanometallic optical antennas, and high diffraction efficiencies have been limited to operation in reflection mode. We describe the experimental realization and operation of dielectric gradient metasurface optical elements capable of also achieving high efficiencies in transmission mode in the visible spectrum. Ultrathin gratings, lenses, and axicons have been realized by patterning a 100-nanometer-thick Si layer into a dense arrangement of Si nanobeam antennas. The use of semiconductors can broaden the general applicability of gradient metasurfaces, as they offer facile integration with electronics and can be realized by mature semiconductor fabrication technologies.

The field of nanophotonics has started to facilitate the replacement of bulky optical components by ultrathin, planar elements (1–5). Such elements can be realized by nanopatterning thin films and can benefit from a more natural integration into electronic and mechanical systems. They can also provide entirely new functions that capitalize on the rapid developments in the field of metamaterials (6). The recent realization of metasurfaces, or metamaterials of reduced dimensionality (7), is of particular relevance as it is opening up new opportunities to realize virtually flat optics (8, 9). Metasurfaces consist of dense arrangements of resonant optical antennas. The resonant nature of the light-matter interaction with such structures affords substantial control over the local light scattering amplitude and phase. These scattering properties can be manipulated through choices of the antenna material, size, geometry, orientation, and environment. By arranging antennas with distinct scattering properties on a surface, space-variant metasurfaces are created that offer tremendous freedom in manipulating optical wave-fronts. Metasurfaces constructed from high-index antenna arrays are used as anti-reflection coatings (10), as well as to enhance absorption (11), create structural color (12), and

manipulate the state of polarization (13, 14). However, space-variant metasurfaces for beam steering and focusing have thus far been constructed from nanoscale metallic antennas only (7). Ohmic losses in the metal and the limited scattering cross sections of the antennas have limited high device efficiencies to reflection mode (15, 16). We leverage recent advances in the realization of high-index dielectric antennas (12, 17, 18) and Pancharatnam-Berry phase optical elements (PBOEs) (19, 20) to realize easy-to-fabricate and highly efficient transmissive devices. Si-based gradient metasurfaces capable of serving as optical gratings, lenses, and axicons are demonstrated.

Figure 1 shows a dielectric gradient metasurface optical element (DGMOE) serving as an axicon. Whereas conventional glass axicons are a few millimeters in size (Fig. 1A), the DGMOE features a 100-nm-thick layer of poly-silicon deposited on a quartz substrate (Fig. 1B) generated in a single patterning step (21). Figure 1D shows a scanning electron microscopy (SEM) image of the fabricated DGMOE composed of thousands of Si nanobeam antennas.

When illuminated with a collimated Gaussian left circularly polarized (LCP) light beam at a 550-nm wavelength, the DGMOE creates a non-diffracting Bessel beam on the transmission (Fig. 1, C and E, and section S2 of the supplementary materials). The intensity distributions along and across the center of Bessel beam are shown as insets to Fig. 1E. The ratio between the high-intensity central beam spot and the first ring is 6:1, a signature of a Bessel beam. The operation of the lens could be analyzed by understanding

all of the coherent far-field and near-field interactions between the Si nanobeam antennas. Here, we describe the behavior of the optical element based on an understanding of the Pancharatnam-Berry (PB) phase.

The PB phase is a geometric phase achieved by space-variant polarization manipulations (22, 23), as opposed to a propagation phase. PBOEs are constructed from wave plate elements for which the orientation of the fast axes depends on the spatial position. Well-defined algorithms exist for realizing specific optical functions. By tiling a surface with half-wave plates with their fast-axes orientations according to a function $\theta(x, y)$, an incident circularly polarized light beam will be fully transformed to a beam of opposite helicity and imprinted with a geometric phase equal to $\varphi_g(x, y) = \pm 2\theta(x, y)$ (21, 24). By controlling the local orientation of the fast axes of the wave plate elements between 0 and π , phase pickups can be achieved that cover the full 0-to- 2π range while maintaining equal transmission amplitude for the entire optical component. This provides full control over the wavefront. A continuous desired phase function can be approximated using discrete wave plate orientations. We use eight orientations with which a high theoretical diffraction efficiency of 95% can be achieved (25). The realization of wave plate elements represents a crucial step in crafting PBOEs.

In designing ultrathin nanobeam-based wave plates, it is important to first understand the optical resonances of individual semiconductor nanobeams. Top-illuminated single beams support resonances under transverse electric (TE) illumination (with the electric field polarized normal to the length of the structure) and the orthogonal transverse magnetic (TM) polarization (12, 18). The thickness of the resonant structures can be small compared with the free-space wavelength due to the high refractive index of semiconductors. A 120-nm-wide and 100-nm-high Si nanobeam supports a strong resonance and a substantial phase retardation in our target wavelength range of interest. We chose this beam as the basic building block for our wave plate (Fig. 2A) in anticipation that its resonant behavior and the accompanied phase retardation between the orthogonal polarizations would persist in the beam array. Finite element simulations indicate that the wavefront for a TE-polarized light beam at 550 nm is delayed by 0.14π as compared with the wavefront in the absence of the nanobeams. The wavefront for TM-polarized light is delayed even further to 1.15π (Fig. 2B). As a result, the phase retardation between the two orthogonal polarizations

¹Geballe Laboratory for Advanced Materials, Stanford University, 476 Lomita Mall, Stanford, CA 94305, USA.

²Micro and Nanooptics Laboratory, Faculty of Mechanical Engineering and Russell Berrie Nanotechnology Institute, Technion-Israel Institute of Technology, Haifa 32000, Israel.

*These authors contributed equally to this work. †Corresponding author. E-mail: brongersma@stanford.edu

is about π , and the beam array serves as a half-wave plate.

By sweeping the wavelength from 490 to 700 nm in simulations, the phase retardation of the wave plate varies from 0.4π to 1.2π (Fig. 2C). For reference, the figure also shows the comparatively small phase retardation of 0.063π for a 100-nm-thick film of calcite, a naturally birefringent crystal. The substantial swing in the phase retardation is attributed to the fact that the nanobeams support a strong fundamental resonance under TE illumination (as seen in absorption) and only a very weak second-order TM resonance (fig. S5D). The order of the resonance is determined by the number of field maxima inside the nanobeam (Fig. 2D, insets). Figure 2C shows that the array's TE resonance and associated swing in the phase retardation can be translated spectrally by changing the beam width.

To realize ultrathin Si nanobeam wave plates, we fabricated the periodic Si nanobeam array described above (Fig. 2C, inset). These samples were characterized optically through measurements of the four Stokes polarization parameters (supplementary materials section S4). The measured phase retardation of this dielectric metasurface is shown by the red squares in Fig. 2C and is in good agreement with optical simulations (red solid line). The transmission coefficient at 550 nm, where the phase retardation is about π , is ~ 0.5 . Spectral transmission measurements show that transmission coefficients as high as 0.75 can be obtained at longer wavelengths (650 to 700 nm) closer to the Si band gap (2I).

The most basic DGMOE is one that serves as a blazed diffraction grating capable of steering a light beam into several diffracted orders. The design follows a general strategy that can be used

to create more complex optical elements. First, Fourier optics is used to determine the phase profile that will produce a desired field distribution in the far field. Blazed gratings feature a simple phase profile with a linear dependence of the phase on position, which either increases or decreases by 2π across one grating period. The desired phase profile is then discretized into segments that can take on a limited number of discrete phases. The discretized profile $\varphi_d(x,y)$ for a grating with a period Λ of $3.2\ \mu\text{m}$ is shown in Fig. 3A. The phase profile is accomplished by tiling a glass substrate with nanobeam wave plates with space-variant orientations (Fig. 3B). To achieve a desired far-field intensity distribution, it is important to control both the metasurface properties and the polarization state of the incident light. For an incident plane wave $|E_{\text{in}}\rangle$ with an arbitrary polarization state, one can show that the output wave $|E_{\text{out}}\rangle$ will be composed of three polarization orders (26)

$$|E_{\text{out}}\rangle = \sqrt{\eta_E}|E_{\text{in}}\rangle + \sqrt{\eta_R}e^{i2\theta(x,y)}|R\rangle + \sqrt{\eta_L}e^{-i2\theta(x,y)}|L\rangle \quad (1)$$

Here, $|R\rangle$ and $|L\rangle$ denote the right- and left-handed circularly polarized unit vectors, respectively. The quantities $\eta_E = |\frac{1}{2}(t_x + t_y e^{i\phi})|^2$, $\eta_R = |\frac{1}{2}(t_x - t_y e^{i\phi})\langle L|E_{\text{in}}\rangle|^2$, and $\eta_L = |\frac{1}{2}(t_x - t_y e^{i\phi})\langle R|E_{\text{in}}\rangle|^2$ provide the magnitude of the coupling efficiencies to the different polarization orders. For convenience, we use Dirac bra-ket notation, where $\langle\alpha|\beta\rangle$ denotes an inner product. The function $\theta(x,y)$ describes the spatially variant distribution of the fast axes of the wave plates. Here, t_x and t_y are the transmission coefficients for light polarized parallel and perpendicular to the fast optical axis, and ϕ is the phase retardation between these linear polarization states. From Eq. 1 it is clear that the optical materials and geometrical properties of the beams, their orientation distribution, and the incident polarization state control the diffraction properties of the array. The operation of DGMOEs can also be explained with simple, intuitive graphics (supplementary materials sections S7 and S8).

The diffraction patterns of the DGMOE blazed grating were observed in transmission with the help of a Bertrand lens (fig. S6). For an incident right circularly polarized (RCP) beam at a wavelength of 550 nm, part of the light changed handedness to LCP and experienced a phase pickup equal to $-2\theta(x,y)$ upon propagation through the DGMOE. As a result, some light steered to the left when viewed from the location of the source (Fig. 3C). A fraction of the light went straight through and emerged again in the incident RCP state due to the fact the transmission magnitudes t_x and t_y are not perfectly equal (fig. S5). For LCP light, part of the light steered to the opposite direction while transforming to RCP light. Again, a fraction of the light went straight through and did not change its state of polarization. For a linearly polarized incident beam, which can be viewed as consisting of equal amounts of RCP and LCP light, light is steered in both directions.

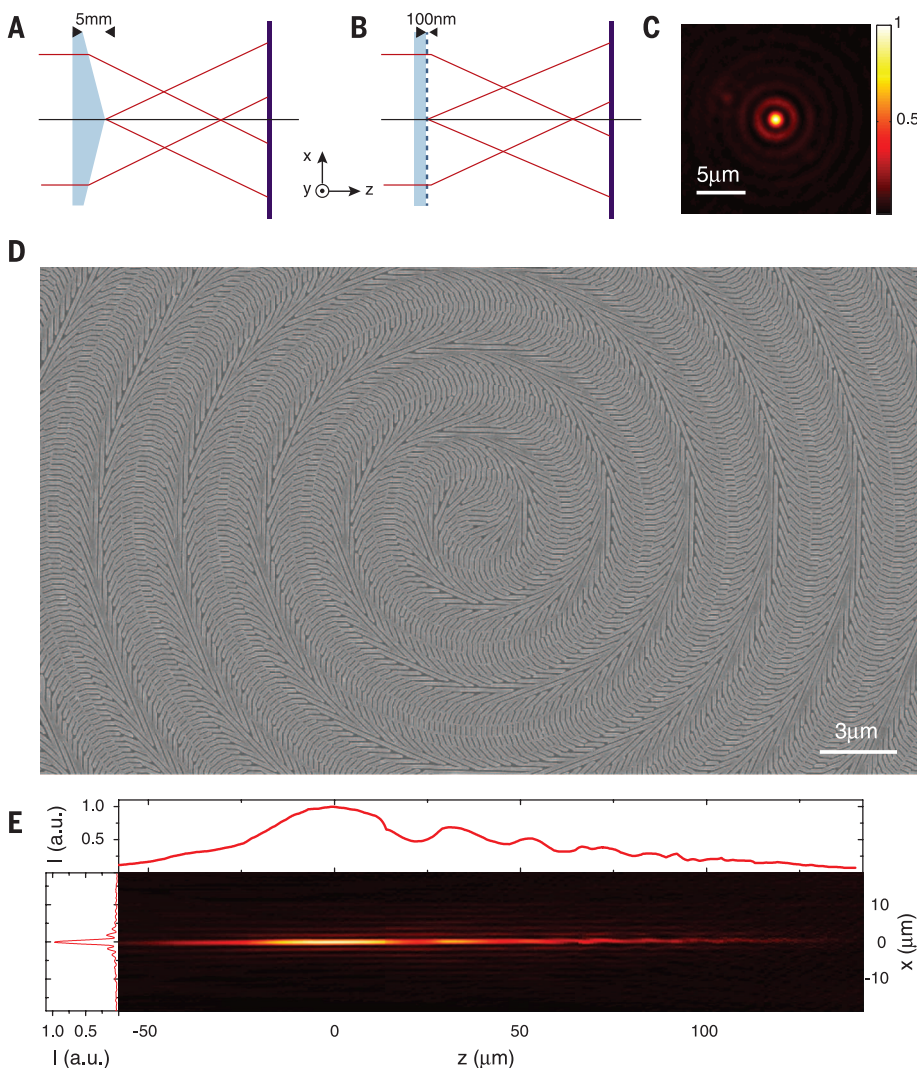


Fig. 1. Example of a DGMOE: An axicon constructed from Si nanoantennas. (A) Schematic of a conventional glass axicon focusing light into a Bessel beam. (B) Schematic of a DGMOE axicon featuring an ultrathin patterned layer of silicon on a quartz substrate. (C) Transversal distribution of Bessel beam generated by the DGMOE. (D) SEM image of the fabricated DGMOE. (E) Measured intensity profile of the nondiffractive Bessel beam generated behind the DGMOE in the xz plane. The intensity (I) along the center of Bessel beam is plotted in the inset along the z axis. The inset along the x axis shows the cross-sectional intensity profile at the $z = 0$ plane. a.u., arbitrary units.

Fig. 2. Ultrathin wave plates constructed from Si nanoantennas.

(A) Schematic view of a periodic Si nanobeam array. **(B)** Phase wavefronts for TE- and TM-polarized, 550-nm-wavelength light upon transmission through a wave plate with 120-nm-wide Si beams. The incident wave without the Si beams is shown for reference. rad, radians. **(C)** Simulated spectra of the phase retardation of a TM-polarized wave with respect to a TE-polarized wave for nanobeam arrays with beam widths of 100 nm (blue), 120 nm (red), 140 nm (green), with the same thickness of 100 nm and duty cycle of 60%. The dashed black line shows the phase retardation for a 100-nm-thick calcite film. Measurements of the phase retardation (red squares) obtained with an array of 120-nm beams show good agreement with the simulations. (Inset) SEM image of the fabricated array. **(D)** Simulated absorption spectra of the 120-nm-wide nanobeam array in (C) under TE (green) and TM (blue) illumination. (Insets) Magnetic field distribution $|H_y|$ for TE and electrical field distribution $|E_x|$ of TM illumination at a wavelength of 600 nm.

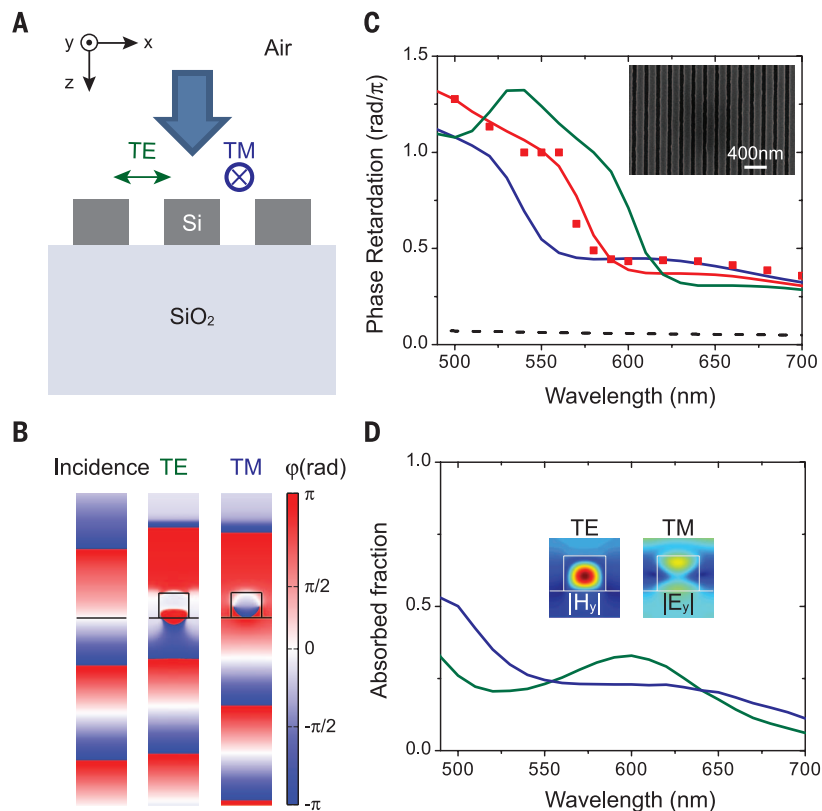
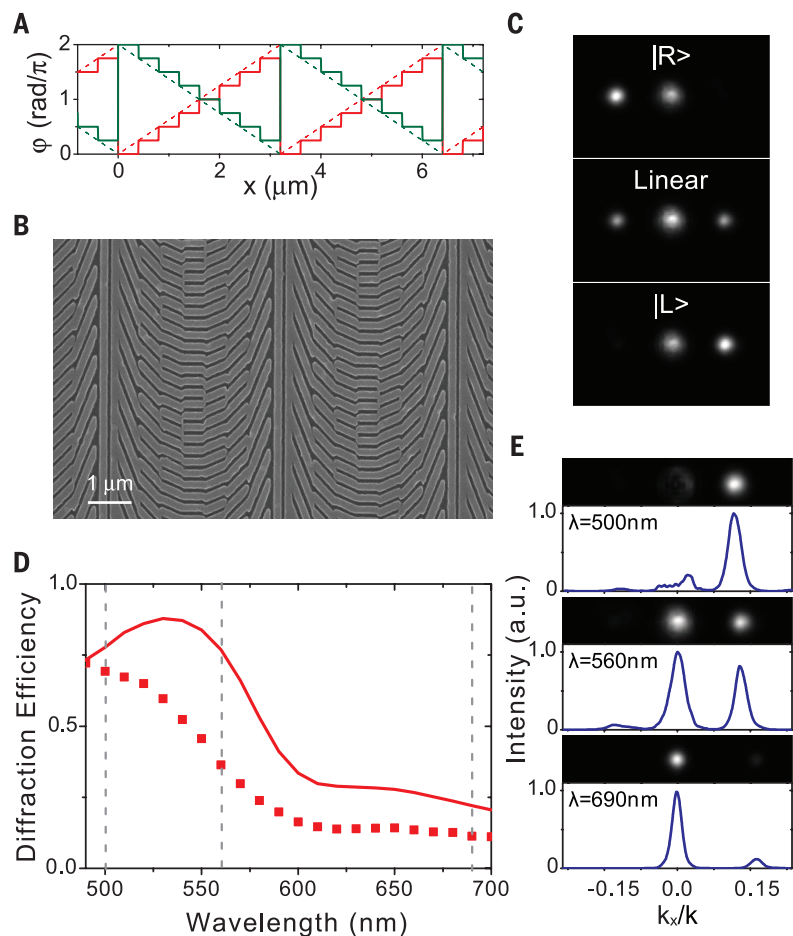


Fig. 3. A DGMOE serving as a blazed grating. **(A)** Discretized (solid line) and continuous (dashed line) phase profile of a DGMOE serving as a blazed grating for illumination with LCP light (red) and RCP light (green). **(B)** SEM image of the fabricated DGMOE. **(C)** Measured diffraction patterns from the DGMOE under illumination with right circular polarization (top), linear polarization (middle), and left circular polarization (bottom) at $\lambda = 550$ nm. **(D)** Theoretical (continuous line) and experimental (solid squares) spectra of diffraction efficiency. **(E)** Measured diffraction patterns of the DGMOE blazed grating and associated cross-sectional intensity distributions versus the normalized in-plane momentum k_x/k under illumination with left circular polarization at wavelengths of 500, 560, and 690 nm [vertical dashed lines in (D)].



The expected polarization states of the transmitted light based on Eq. 1 were successfully verified by adding a circular polarizer on the transmission side of the metasurface (supplementary materials section S4 and movie S2). These observations demonstrate the possibility to steer light by changing the incident polarization (movie S1).

DGMOEs can operate over a broadband wavelength range, and it is thus important to understand their wavelength-dependent properties. Because the geometric phase depends only on the orientation function θ , the phase profile experienced by RCP and LCP light will remain the same at each wavelength. This does not imply that the diffraction properties stay the same as well. For example, the steering angle of the blazed grating α increases for longer wavelengths, as this quantity is determined by the ratio of the wavelength and grating period ($\sin \alpha = \lambda/\Lambda$). The diffraction efficiency also varies across the spectrum, as it is linked to the wavelength-dependent transmission and phase-retardation properties of the nanobeam wave plates. The diffraction efficiency η_D is defined by

the ratio of the power of circularly polarized light that has been converted to the opposite helicity (i.e., experiencing phase pickup) and the total transmitted power that is transmitted through the metasurface. For a well-designed blazed grating, the intensity in higher diffraction orders is very weak. As such, the total power of transmitted light is approximately equal to the sum power of the zero-order intrinsic beam and the first-order converted beam: $\eta_D \approx I_{1st}/(I_{1st} + I_{0rd})$. The diffraction efficiency for the grating shown in Fig. 3B was determined by measuring the light intensity of the through beam and the diffracted beam with a calibrated charge-coupled device camera (supplementary materials section S6). Figure 3D shows the experimental diffraction efficiency spectra for normally incident LCP light in the wavelength range from 490 to 700 nm (red squares). It also shows theoretical efficiencies calculated using the expressions for η_E and η_R given below Eq. 1. These efficiencies were determined using the measured values of t_{cs} , t_p , and ϕ and by taking into account the expected diffraction efficiency of 95% that is appropriate for an eight-level phase discretization.

The experimental diffraction patterns at three different wavelengths are plotted in Fig. 3E. At a wavelength of 500 nm, 75% of the light is steered, and the intensity of the zero-order beam (i.e., the straight-through beam) is very low compared with that of the first diffracted order. In contrast, at $\lambda = 690$ nm only a small portion of light is steered, and most of the energy remains in the zero-order beam. The pattern also shows the expected increase in the steering angle at this longer wavelength. The overall shape of the measured efficiency spectrum qualitatively agrees with the predicted spectrum, but the measured efficiencies tend to be lower, possibly attributed to imperfections in the fabricated structure. Alternatively, it may be that the birefringent nature of the nanobeam wave plates is size-dependent.

We also realized a DGMOE serving as a conventional lens (Fig. 4A). The phase profile for this DGMOE lens again features eight discrete levels and approximates a hyperboloidal phase profile (supplementary materials section S9). The lens features a focal length of 100 μm and a numerical aperture (NA) of 0.43 at a wavelength of 550 nm. When the DGMOE is uniformly illuminated from the substrate side with RCP light, it concentrates light into a LCP focal spot (Fig. 4B and see supplementary materials section S2 for details). The focal spot size measures 670 nm in full width at half maximum, close to the diffraction-limited spot size.

The presented design principles are generally applicable to any high-index semiconductor or insulator and can be applied at any desired wavelength. The lowest ohmic losses were achieved near the semiconductor band edge. The presented ultrathin DGMOEs address an increased need for low-cost, lightweight, and compact optical elements that can easily be integrated into complex systems requiring assembly of optical, electronic, and mechanical components.

REFERENCES AND NOTES

1. L. Verslegers *et al.*, *Nano Lett.* **9**, 235–238 (2009).
2. D. Fattal, J. Li, Z. Peng, M. Fiorentino, R. G. Beausoleil, *Nat. Photonics* **4**, 466–470 (2010).
3. C. J. Chang-Hasnain, *Semicond. Sci. Technol.* **26**, 014043 (2011).
4. F. Afshinmanesh, J. S. White, W. Cai, M. L. Brongersma, *Nanophotonics* **1**, 125–129 (2012).
5. E. T. F. Rogers *et al.*, *Nat. Mater.* **11**, 432–435 (2012).
6. N. Engheta, *Science* **317**, 1698–1702 (2007).
7. A. V. Kildishev, A. Boltasseva, V. M. Shalaev, *Science* **339**, 1232009 (2013).
8. N. Yu *et al.*, *Science* **334**, 333–337 (2011).
9. X. Ni, N. K. Emani, A. V. Kildishev, A. Boltasseva, V. M. Shalaev, *Science* **335**, 427 (2012).
10. P. Spinelli, M. A. Verschuuren, A. Polman, *Nat. Commun.* **3**, 692 (2012).
11. L. Cao *et al.*, *Nano Lett.* **10**, 439–445 (2010).
12. L. Cao, P. Fan, E. S. Barnard, A. M. Brown, M. L. Brongersma, *Nano Lett.* **10**, 2649–2654 (2010).
13. Y. Yang *et al.*, *Nano Lett.* **14**, 1394–1399 (2014).
14. C. Wu *et al.*, <http://arxiv.org/abs/1309.6616> (2013).
15. A. Pors, O. Albrektsson, I. P. Radko, S. I. Bozhevolnyi, *Sci. Rep.* **3**, 2155 (2013).
16. S. Sun *et al.*, *Nano Lett.* **12**, 6223–6229 (2012).
17. R. K. Mongia, A. Iltipiboon, *IEEE Trans. Antenn. Propag.* **45**, 1348–1356 (1997).
18. L. Cao *et al.*, *Nat. Mater.* **8**, 643–647 (2009).

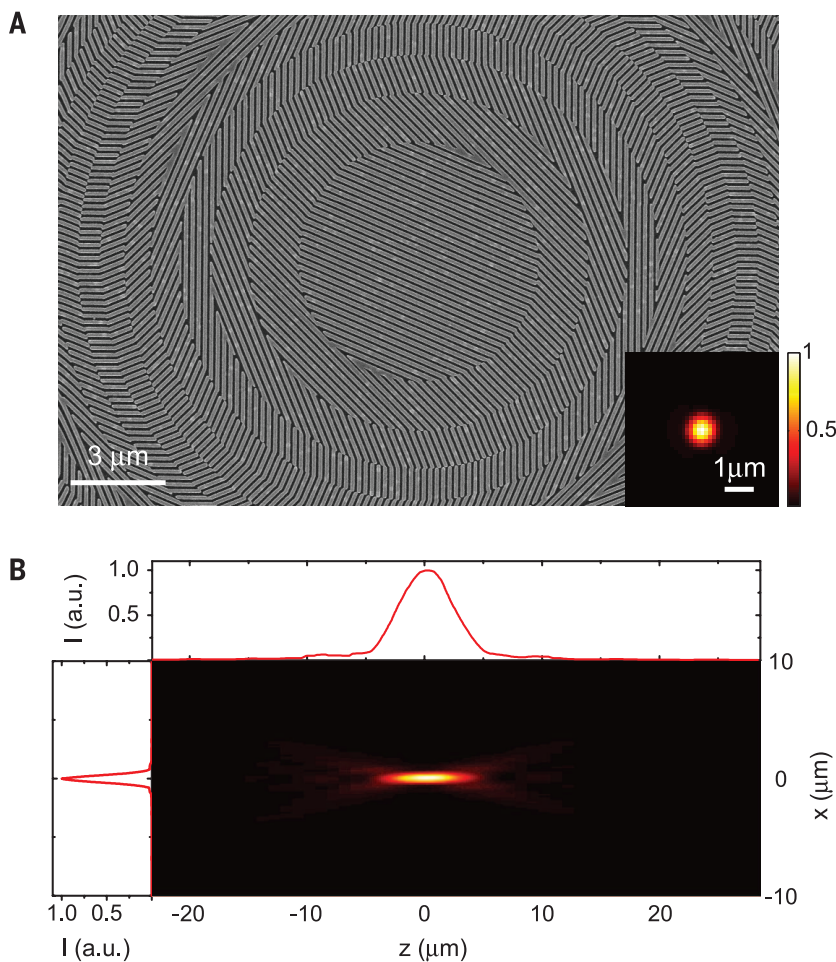


Fig. 4. A DGMOE lens based on Si nanobeams. (A) SEM image of a fabricated DGMOE lens with a focal length of 100 μm at $\lambda = 550$ nm. (Inset) Two-dimensional intensity profile in the focal plane. **(B)** Measured intensity profile generated behind the DGMOE in the xz plane. The intensity distributions along the optical axis and through the focus are shown along the vertical and horizontal axes.

19. Z. Bomzon, G. Biener, V. Kleiner, E. Hasman, *Opt. Lett.* **27**, 285–287 (2002).
 20. A. Niv, G. Biener, V. Kleiner, E. Hasman, *Opt. Lett.* **29**, 238–240 (2004).
 21. Materials and methods are available as supplementary materials on Science Online.
 22. S. Pancharatnam, *Proc. Indiana Acad. Sci.* **A44**, 247–262 (1956).
 23. M. V. Berry, *J. Mod. Opt.* **34**, 1401–1407 (1987).
 24. Z. Bomzon, G. Biener, V. Kleiner, E. Hasman, *Opt. Lett.* **27**, 1141–1143 (2002).

25. A. Niv, G. Biener, V. Kleiner, E. Hasman, *Opt. Commun.* **251**, 306–314 (2005).
 26. E. Hasman, V. Kleiner, G. Biener, A. Niv, *Appl. Phys. Lett.* **82**, 328–330 (2003).

ACKNOWLEDGMENTS

We acknowledge funding support from the Global Climate and Energy Project. P.F. acknowledges support from the Stanford Graduate Fellowship. We also thank P. Landreman for his assistance with the optical measurements.

SUPPLEMENTARY MATERIALS

www.sciencemag.org/content/345/6194/298/suppl/DC1
 Materials and Methods
 Figs. S1 to S10
 References (27–30)
 Movies S1 to S3

11 March 2014; accepted 2 June 2014
 10.1126/science.1253213

QUANTUM COMPUTING

Quantum computations on a topologically encoded qubit

D. Nigg,^{1*} M. Müller,^{2*} E. A. Martinez,¹ P. Schindler,^{1,†} M. Hennrich,¹ T. Monz,¹ M. A. Martin-Delgado,² R. Blatt^{1,3}

The construction of a quantum computer remains a fundamental scientific and technological challenge because of the influence of unavoidable noise. Quantum states and operations can be protected from errors through the use of protocols for quantum computing with faulty components. We present a quantum error-correcting code in which one qubit is encoded in entangled states distributed over seven trapped-ion qubits. The code can detect one bit flip error, one phase flip error, or a combined error of both, regardless on which of the qubits they occur. We applied sequences of gate operations on the encoded qubit to explore its computational capabilities. This seven-qubit code represents a fully functional instance of a topologically encoded qubit, or color code, and opens a route toward fault-tolerant quantum computing.

A fully fledged quantum computer can be used to efficiently solve notoriously difficult problems, such as factoring large numbers or simulating the dynamics of many-body quantum systems (1). Technological progress has enabled the implementation of small-scale prototype quantum computing devices on diverse physical platforms (2). Sophisticated fault-tolerant quantum computing (FTQC) techniques have been developed for the systematic correction of errors that dynamically occur during storage and manipulation of quantum information (3–5). For quantum error correction, Calderbank-Shor-Steane (CSS) codes (4, 5) enable independent detection and correction of bit and phase flip errors, as well as combinations thereof. Furthermore, quantum information processing is substantially facilitated in quantum codes in which logical operations on encoded qubits are realized by the bitwise application of the corresponding operations to the underlying physical qubits (i.e., in a transversal way). This property prevents uncontrolled propagation of errors through the quantum hardware, which in turn is essential to enter the FTQC regime (1). Ultimately, reliable quantum memories and arbitrarily long quan-

tum computations are predicted to become feasible for appropriately designed quantum codes, once all elementary operations are realized in a fault-tolerant way and with sufficiently low error rates (6, 7).

To date, topological quantum computing represents the most promising and realistic approach toward FTQC. In this method, the encoding of quantum information in global properties of a many-particle system provides protection against noise sources that act locally on individual or small sets of qubits (8). Most prominently, topological quantum computing offers highly competitive error thresholds as high as 1% per operation (9–12), which is within reach of current experimental capabilities (13–15) and typically about two orders of magnitude larger than in schemes using concatenated quantum codes (7).

Within topological quantum computing, topological color codes (16, 17) offer the distinctive feature that the entire group of Clifford gate operations, allowing for arbitrary 90° and 180° qubit rotations, can be implemented transversally (1). This versatile set of operations directly enables protocols for quantum distillation of entanglement, quantum teleportation, and dense coding with topological protection (16). Moreover, a universal gate set, enabling the implementation of arbitrary quantum algorithms, can be achieved by complementing the Clifford operations with a single non-Clifford gate (1). For color codes in two-dimensional (2D) architectures (16), such an additional gate can be realized by a technique known as magic-state injection (18). Remarkably,

this method is not needed in 3D color codes that enable implementation of a universal gate set using exclusively transversal operations (17).

Previous experiments have demonstrated the correction of a single type of error by the three-qubit repetition code (19–21), correction of bit and phase flip errors by the non-CSS-type five-qubit code in nuclear magnetic resonance systems (22, 23), as well as elements of topological error correction in the framework of measurement-based quantum computation (24). Here, we demonstrate a quantum error-correcting seven-qubit CSS code (5), which is equivalent to the smallest instance of a 2D topological color code (16). The application of multiple operations from the entire, transversally implemented set of logical single-qubit Clifford gates represents the realization of quantum computations on a fully correctable encoded qubit.

Two-dimensional color codes are topological quantum error-correcting codes that are constructed on underlying 2D lattices (16) for which three links meet at each vertex and three different colors are sufficient to assign color to all polygons (plaquettes) of the lattice, such that no adjacent plaquettes sharing a link are of the same color. The smallest fully functional 2D color code involves seven qubits (Fig. 1A) and consists of a triangular, planar code structure formed by three adjoined plaquettes with one physical qubit placed at each vertex. Color codes are stabilizer quantum codes (1, 25), which are defined by a set of commuting, so-called stabilizer operators $\{S_i\}$, each having eigenvalues +1 or -1. More precisely, the code space hosting logical or encoded quantum states $|\psi\rangle_L$ is fixed as the simultaneous eigenspace of eigenvalue +1 of all stabilizers, $S_i|\psi\rangle_L = +|\psi\rangle_L$. In color codes, there are two stabilizer operators associated with each plaquette, which for the seven-qubit color code (Fig. 1A) results in the set of four-qubit X and Z -type operators

$$\begin{aligned} S_x^{(1)} &= X_1 X_2 X_3 X_4 & S_z^{(1)} &= Z_1 Z_2 Z_3 Z_4 \\ S_x^{(2)} &= X_2 X_3 X_5 X_6 & S_z^{(2)} &= Z_2 Z_3 Z_5 Z_6 \\ S_x^{(3)} &= X_3 X_4 X_6 X_7 & S_z^{(3)} &= Z_3 Z_4 Z_6 Z_7 \end{aligned} \quad (1)$$

where X_b , Y_b , and Z_i denote the standard Pauli matrices acting on the i th physical qubit with the computational basis states $|0\rangle$ and $|1\rangle$ (1). The stabilizers in Eq. 1 impose six independent constraints on the seven physical qubits and thus define a two-dimensional code space, which allows the encoding of one logical qubit. The logical basis states $|0\rangle_L$ and $|1\rangle_L$ spanning the code space are entangled seven-qubit states and

¹Institut für Experimentalphysik, Universität Innsbruck, A-6020 Innsbruck, Austria. ²Departamento de Física Teórica I, Universidad Complutense, 28040 Madrid, Spain. ³Institut für Quantenoptik und Quanteninformation der Österreichischen Akademie der Wissenschaften, A-6020 Innsbruck, Austria. *Corresponding author: E-mail: daniel.nigg@uibk.ac.at (D.N.); mueller@ucm.es (M.M.) †These authors contributed equally to this work. ‡Present address: Department of Physics, University of California, Berkeley, CA 94720, USA.



Dielectric gradient metasurface optical elements

Dianmin Lin, Pengyu Fan, Erez Hasman and Mark L. Brongersma
(July 17, 2014)

Science **345** (6194), 298-302. [doi: 10.1126/science.1253213]

Editor's Summary

Extending the range of planar optics

To build miniature optical devices, scientists are using silicon to replace bulky three-dimensional devices with flat versions. A patterned surface consisting of dense arrays of nanoscale silicon strips, which act as antennae, can be designed to work as transparent optical devices for the manipulation of light. Lin *et al.* used their versatile patterning technique to create a suite of planar optical elements. By patterning a 100-nm layer of silicon into a dense arrangement of nano-antennae, they were able to fabricate gratings, lenses, and axicons—a device that can add a shape to a propagating light beam.

Science, this issue p. 298

This copy is for your personal, non-commercial use only.

- Article Tools** Visit the online version of this article to access the personalization and article tools:
<http://science.sciencemag.org/content/345/6194/298>
- Permissions** Obtain information about reproducing this article:
<http://www.sciencemag.org/about/permissions.dtl>

Science (print ISSN 0036-8075; online ISSN 1095-9203) is published weekly, except the last week in December, by the American Association for the Advancement of Science, 1200 New York Avenue NW, Washington, DC 20005. Copyright 2016 by the American Association for the Advancement of Science; all rights reserved. The title *Science* is a registered trademark of AAAS.